Supporting Information

Haoyu Zhao[a], Guiyong Chen[b], Yusong Ma[a], Rongting Guan[a], YiGe Han[a]，Feng Chen[a*], Weiwei Xu[b], Yuhang Liu[b]

[a] College of Polymer Science and Engineering, Sichuan University, ChengDu610065, China

[b] AVIC Chengdu Aircraft Industrial (Group) Co. Ltd, Chengdu, 610091

Characterization

CB exhibits aggregation tendencies in solution. To evaluate the dispersion stability, SDS is introduced into the system as dispersant combined with mechanical dispersion at varying mass ratios relative to CB (10%, 11.8%, 14.3%, 18.2%, and 25%). The dispersion efficacy was quantified through time-dependent solution conductivity measurements. As evidenced by Fig. S1a and S1b, CB sedimentation inevitably occurs, resulting in a reduced particle suspension and decrease in conductivity. However, optimized SDS concentrations effectively stabilize solution conductivity within 10 minutes, confirming CB stable dispersion.

SDS function is an anionic dispersant, inducing electrostatic repulsion between CB particles through charge polarization. Concurrently, SDS content also influences solution viscosity, which influences coating adhesion efficiency. Fig. S1d and S1e reveal more than 14.3% of the content, the viscosity of the solution decreases significantly. The improvement of the CB aggregation phenomenon results in better dispersion. Furthermore, Fig. S1f demonstrates enhanced wall-adhesion uniformity in SDS-modified solutions, exhibiting reduction in surface roughness and suppressed particle agglomeration.

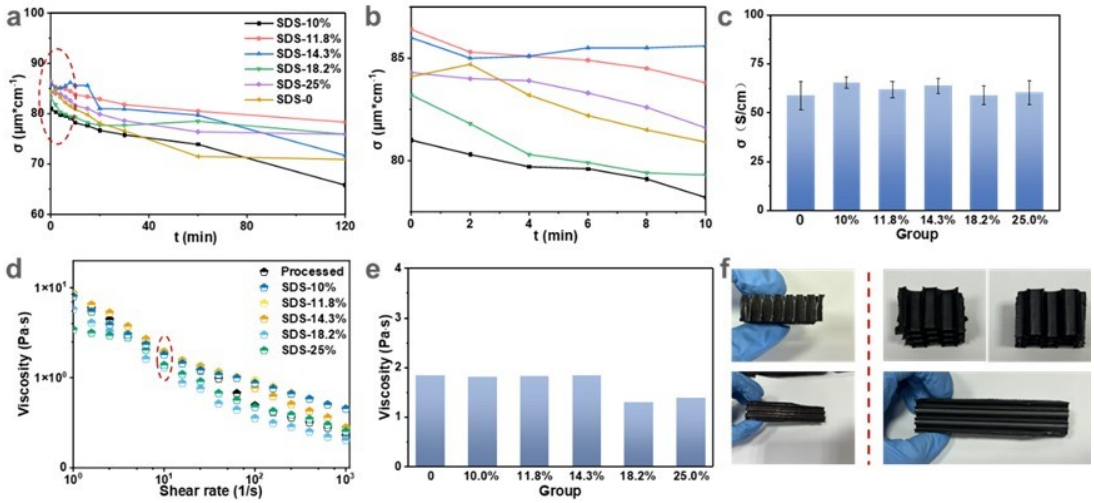

Fig. S1. (a)(b) Influence of SDS on the solution conductivity of CB-phenolic composites; (c) impact of SDS on the solid-state conductivity of CB-phenolic films; (d)(e) SDS-induced variations in shear viscosity of CB-phenolic solutions; (f) visual comparison of CB dispersion effectiveness.

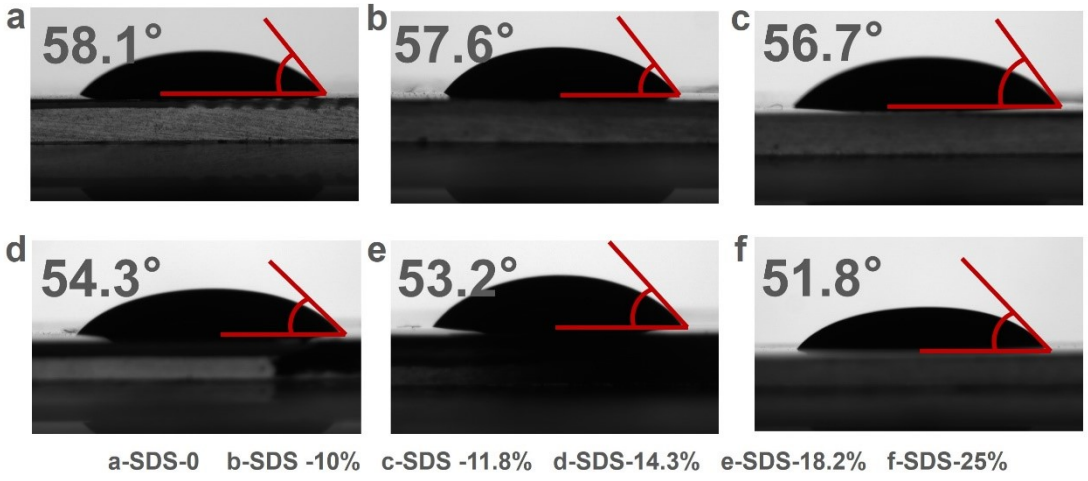

Fig. S2. Influence of SDS concentration on the interfacial wettability between carbon black (CB) dispersions and phenolic resin.

Fig. S3 shows the prepared CB slurry controls the layer wall thickness through different impregnation cycles, affecting the overall performance.

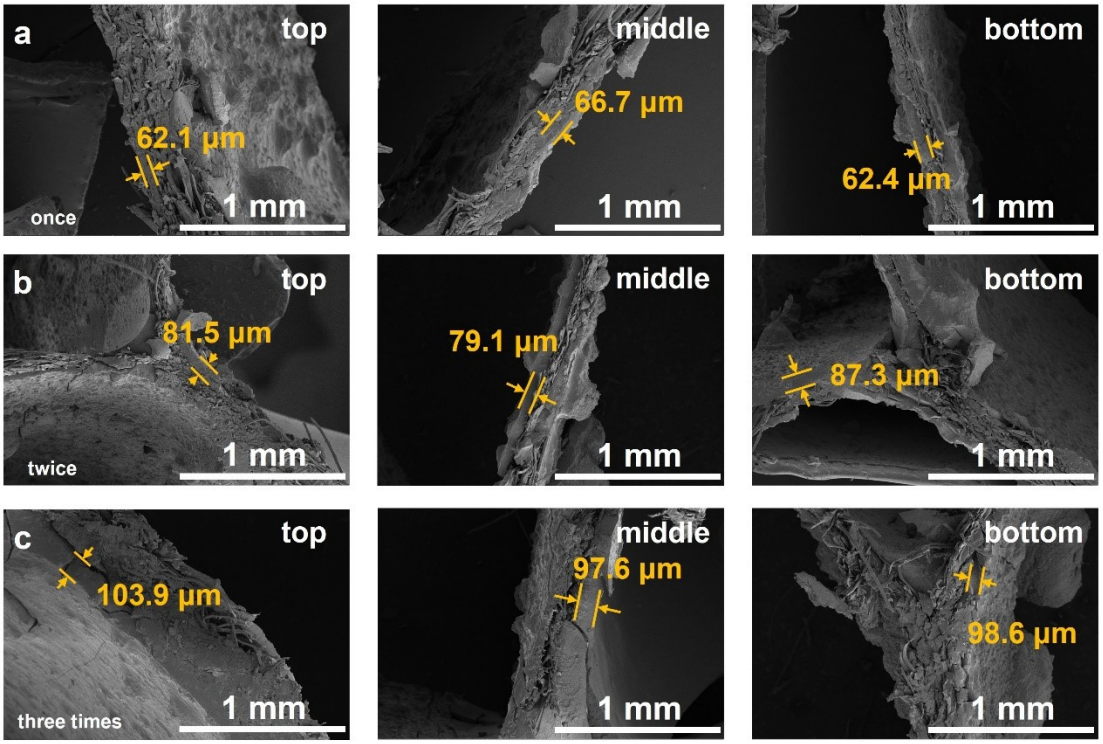

Fig. S3. SEM images of impregnation 110mm-high honeycomb section (Three structural segments: top, middle, and bottom) by (a) once, (b) twice and (c) three times impregnation.

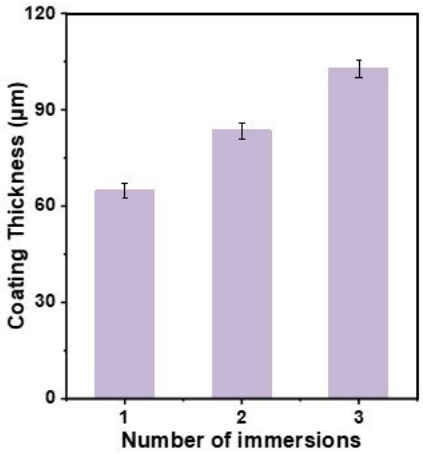

Fig. S3 (inset) Coating thickness statistics for each sample.

Table S1 and S2 show the statistical data of the adhesive properties and attachment amounts of the slurry with different additive contents at two different heights. It can be observed that the addition of SDS makes the attachment percentage of the slurry more uniform across different heights.

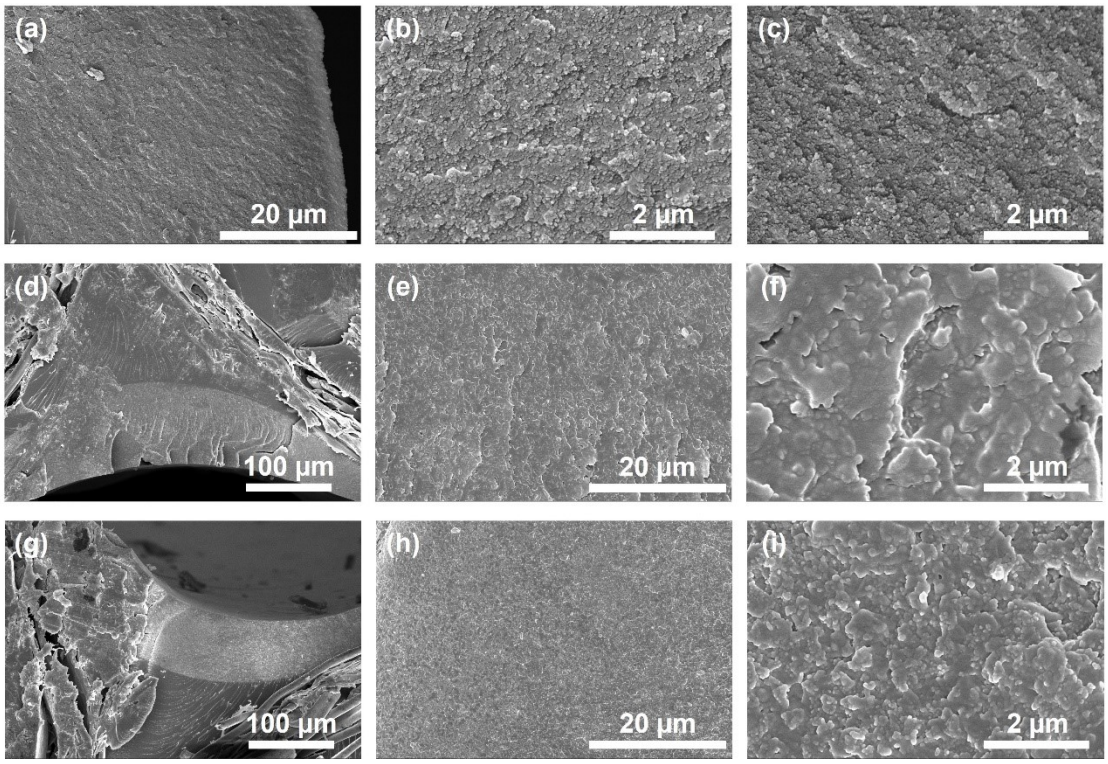

Fig S4. (a-c) Distribution of the CB coating on the cross section of the honeycomb wall; (d-i) Distribution of the CB coating at the corners of the honeycomb.

Table S1. Influence of SDS concentration on single impregnation resin loading in 10mm-high honeycomb composite

	Blank honeycomb			0	10%	11.8 %	14.3%	18.2%	25%
Blank/g	2.63	1.3	0.3	0.3	1.6	2.0	0.3	0.7	0.6
Impregnated/g	3.6	2.4	0.6	0.5	2.5	3.0	0.4	1.2	0.9
Weight increase/%	60.2	81.7	127.5	100.0	55.2	50.5	55.3	59.7	66.1

Table S2. Influence of SDS concentration on single impregnation resin loading in 110mm-high honeycomb composite

	Blank honeycomb	0	10%	11.8	14.3%	18.2%	25%

						%			
Blank/g	5.2	3.3	2.4	4.6	4.1	5.4	5.2	5.5	3.9
Impregnated/g	7.9	4.7	3.8	9.4	7.3	8.2	8.2	9.8	7.2
Weight increase/%	51.3	50.1	62.4	101.7	78.1	51.7	58.8	78.9	81.6

The wall thickness of wave-absorbing impregnated layers is precisely regulated by adjusting phenolic solution solubility and impregnation cycles to formulate carbon black (CB) dispersions. Figure 1 delineates the hierarchical wall thickness profiles of fabricated multilayer honeycomb composites. As demonstrated in Fig. 1(a)-(e), specimens with 10 wt.% phenolic concentration exhibit uniform surface coatings, achieving a wall thickness of 47.53 μm. For 12 wt.% formulations, distinct thickness gradients are observed (49.86 μm and 60.29 μm), while 15 wt.% variants display further augmented dimensions (61.55 μm and 75.59 μm), confirming the concentration-dependent growth kinetics of impregnated layers. This methodology establishes a quantitative correlation between solution viscosity, impregnation parameters, and geometric precision of microwave-absorbing architectures.

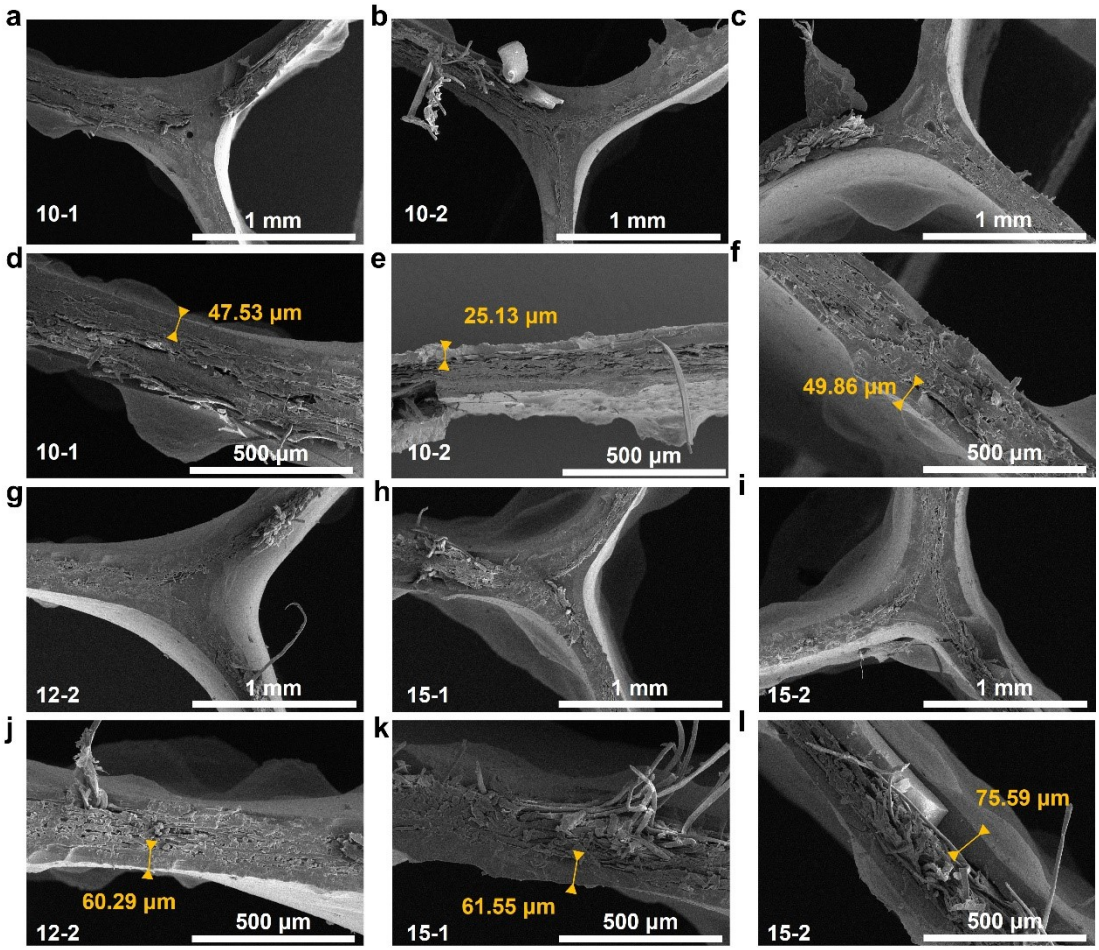

Fig. S5. (a)(c) SEM images of 10wt%-1 phenolic-impregnated honeycomb section; (b)(e) SEM images of 10wt%-2 phenolic-impregnated honeycomb section; (c)(f) SEM images of 12wt%-1 phenolic-impregnated honeycomb section; (g)(j) SEM images of 12wt%-2 phenolic-impregnated honeycomb section; (h)(k) SEM images of 15wt%-1 phenolic-impregnated honeycomb section; (i)(l) SEM images of 15wt%-2 phenolic-impregnated honeycomb section.

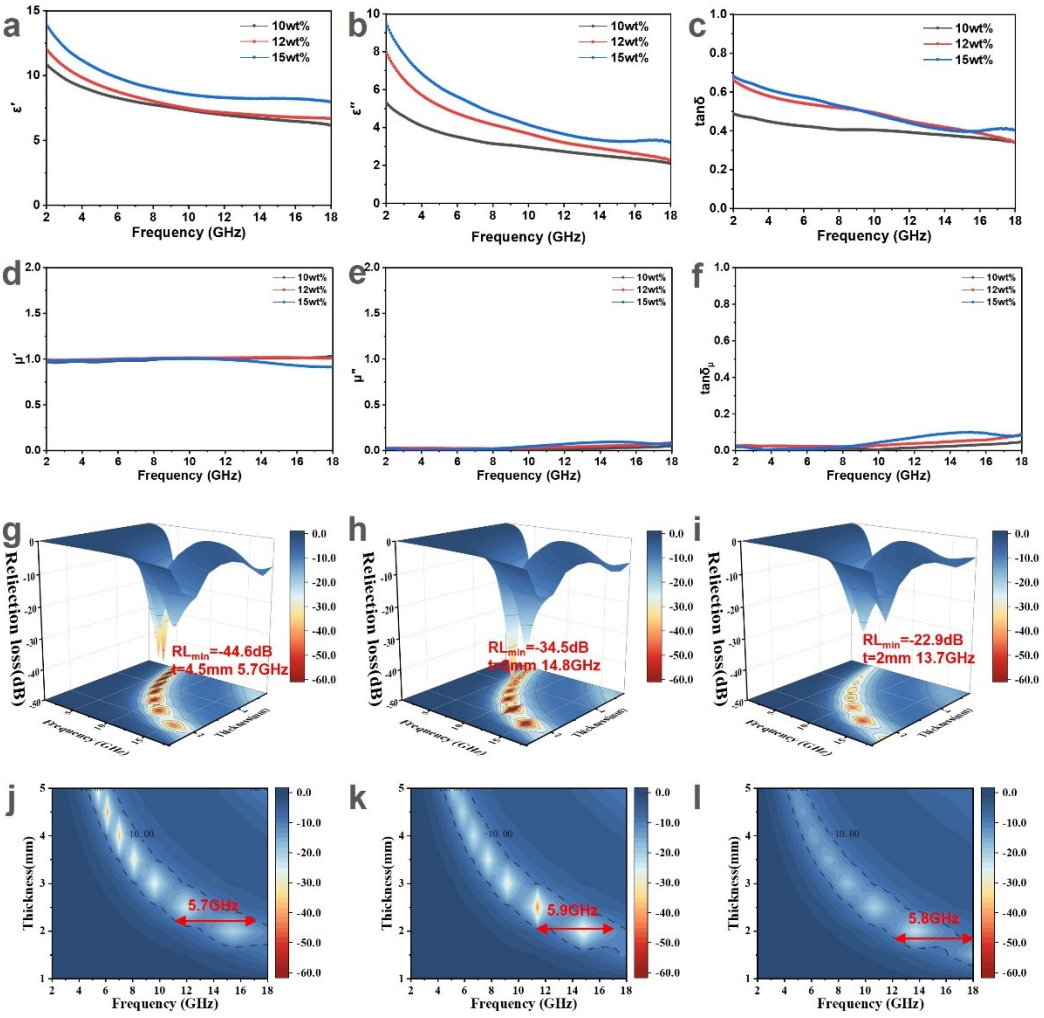

Fig. S6. (a) Electromagnetic parameters of composites with varying CB concentrations: ε' (a) and ε'' (b); (c) dielectric loss tangent with varying CB concentrations; 3D plot of Reflection Loss (RL) for CB at (d) 10 wt.%, (e) 12 wt.% and (f) 15 wt.%; effective absorption bandwidth (EAB) plot of CB at (g) 10 wt.%, (h) 12 wt.%, and (i) 15 wt.%.

Fig. S7 systematically compares the CST-simulated electric field (|E|) and power loss distributions of IAH-111 and IAH-112 specimens, revealing consistent electromagnetic response patterns across IAH-122 and IAH-121 samples. The topological similarity in |E| distributions confirms that the impedance matching mechanism in honeycomb-structured metamaterial coatings is predominantly governed by two structural-electromagnetic parameters: honeycomb height and incident wave

frequency. Power loss analysis at 4.8 GHz demonstrates that thickness variations in the base honeycomb layer disrupt interlayer impedance matching. Notably, IAH-112 exhibits extended interfacial loss zones (green-domain expansion) at layer junctions due to its superior conductivity and progressive migration of dissipation cores toward honeycomb wall midplanes. This frequency-selective behavior persists at 10GHz and 14.2 GHz, where enhanced electromagnetic energy dissipation is evidenced by expanded absorption coverage and intensified power loss.

All specimens exhibit frequency-dependent field regulation: with increasing frequency induces periodic electric field and power loss patterns emerge within the honeycomb units. High frequency regimes trigger energy localization at wall mid-regions, accompanied by intensified multi-reflective interactions near honeycomb bases, which is reflected as the more red parts in the Power Loss.

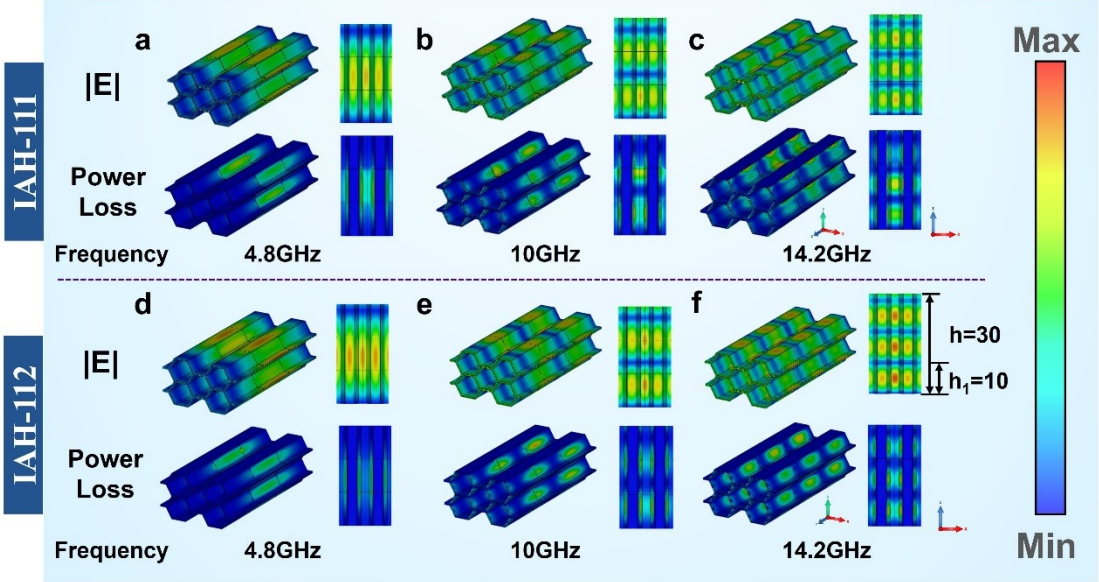

Fig. S7. (a-c) Electric field (|E|) and Power Loss distributions of IAH-111 honeycomb composites in the frequencies of 4.8 GHz, 10 GHz and 14.2 GHz; (d-f) Electric field (|E|) and Power Loss distributions of IAH-111 honeycomb composites in the frequencies of 4.8 GHz, 10 GHz and 14.2

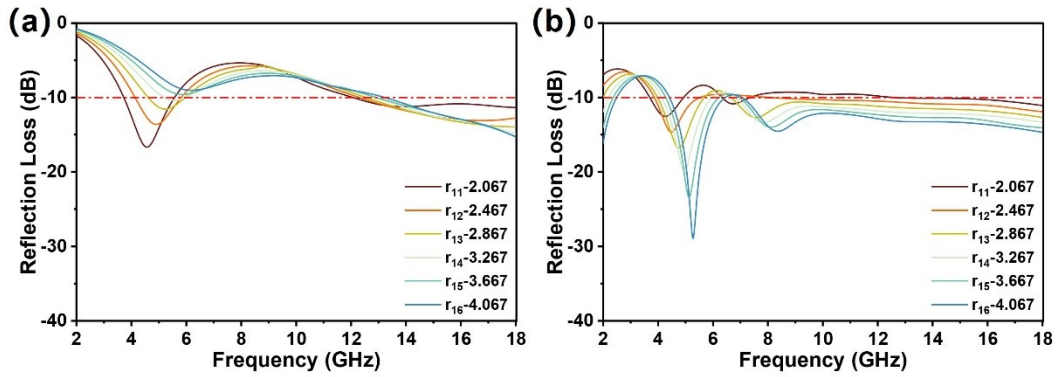

Fig. S8. (a) RL performance variation of 10 mm honeycomb at different radius; (b) RL performance variation of 30 mm honeycomb at different radius (coating thickness is 100 μm for all)